Manipulation of Evanescent Wave Coupling in High-Q Terahertz All-Dielectric Metasurfaces

Song Han, *Member, IEEE*

***Abstract*—The resonance characteristics in periodically arranged artificial dielectric photonics and metasurfaces have attracted interests due to their growing applications in filters, low-threshold lasers, nonlinear generation of light, waveguides, chemical and biological sensors. Here, we experimentally demonstrate a family of silicon-based terahertz metasurfaces supporting high-Q resonances that is illustrated theoretically by the extended Marcatili's analysis in periodic boundary condition. We further reveal that the evanescent wave coupling along the direction of incident electric field merely radiate EM energy. Therefore, the vary of geometric parameter along such direction mainly change the resonance frequencies of the cuboid-based dielectric metasurface, while the resonant amplitudes and Q-factors at different geometric parameters are almost the same. Such characteristics is highly promising for application of on-chip THz/mid-IR spectrometer by spatially arranging different cuboid-based dielectric metasurfaces with scaled dimensions. The extended Marcatili's analysis shown here could further enable design of flat nanoscale metasurfaces for optical applications.**

***Index Terms*—Evanescent wave coupling, terahertz all-dielectric metasurfaces, high-Q resonances.**

I. Introduction

STRONG light localization in resonant subwavelength micro-nanostructures is extremely important for various applications in optics and photonics including lasing [1], [2], [3], sensing [4], harmonic generation [5], [6], [7], [8], [9], [10], Raman scattering [11], and photovoltaics [12]. Plasmonic resonances with metal nanostructures have been extensively studied for the large confinement of light at the deep subwavelength scale [13], [14], [15], [16]. However, inevitable Ohmic losses in these plasmonic structures set the bottleneck for realizing higher quality (Q) factor resonances that limits the performance efficiency of photonic devices. High-refractive-index dielectric resonators offer a novel route for the subwavelength confinement of light by inducing the Mie resonances that only suffer from the radiation damping [1], [2], [3], [4], [5], [6], [7], [8], [17], [18], [19], [20], [21], [22]. Such resonators exhibit electric and magnetic dipole, as well as higher order Mie resonances where the absorption loss is negligible.

Even though the micro-nanoparticles made of conventional high-refractive-index semiconductors such as silicon, germanium, and gallium arsenide have low absorptive losses, the Q-factor is relatively low ($Q < 10$) due to the strong radiative losses under the prediction of the standard Mie theory [17], [18], [19], [20]. All-dielectric metamaterial, with the freedom of artificially designed configuration, is one of many exciting alternatives for suppressing the radiative losses by properly tailoring the unit cell geometries as well as the spatial arrangement, so as to achieve extremely high-Q resonance. For instance, a dielectric anapole with spectral overlap of electric and toroidal dipole modes lead to a strong suppression of the dominant electric dipole scattering due to destructive interference and enabled resonant Q-factor larger than 30 [11]. At infrared (IR) regime, a Q-factor of 127 has been experimentally demonstrated using silicon (Si) based asymmetric cut-wire metamaterials [21], and a sharper transparency window with a Q-factor of 483 was discovered in a coupled bright-dark mode system [4]. In the visible regime [22], a thin photonic crystal slab with patterned Ta_2O_5 nanorod on a flexible substrate has been proposed to functionalize as a mechanically tunable color filter with a simulated Q-factor of up to 800. In most of these previous demonstrations, a large array size was designed to reduce the light scattering due to lattice perturbations at the edge of the array. This provided the enhancement in the collective response, i.e., coherence of the metamaterials, and thus reduced the radiative losses for acquiring high Q-factors [4].

Apart from the visible and IR regimes of the electromagnetic spectrum, terahertz (THz) radiation is a specific frequency range that falls in between infrared and microwave radiation. THz regime has attracted enormous attention in the recent years due to its unique properties such as nonionizing photon energy, spectral fingerprints of intermolecular vibrations, and high transparency of optically opaque materials, thereby making it highly desirable for applications in biological sensing, material analysis, and imaging [23]. However, THz all-dielectric metamaterials with high-Q resonances have received less attention in the literature. Most dielectric materials and intrinsic semiconductors have negligible absorption losses in THz and IR regions, which provides good opportunities for designing extremely high-Q metamaterials and photonic devices. This would open a huge

Manuscript received 15 July 2023; revised 10 August 2023; accepted 12 August 2023. Date of publication 16 August 2023; date of current version 25 August 2023. This work was supported by the Start-Up Foundation for the "Hundred Talents Program" from Zhejiang University.

The author is with the ZJU-Hangzhou Global Scientific and Technological Innovation Center, Zhejiang University, Hangzhou 311215, China, and also with the Interdisciplinary Center for Quantum Information, State Key Lab. of Modern Optical Instrumentation, College of Information Science and Electronic Engineering, Zhejiang University, Hangzhou 310027, China (e-mail: song.han@zju.edu.cn).

Digital Object Identifier 10.1109/JPHOT.2023.3305581

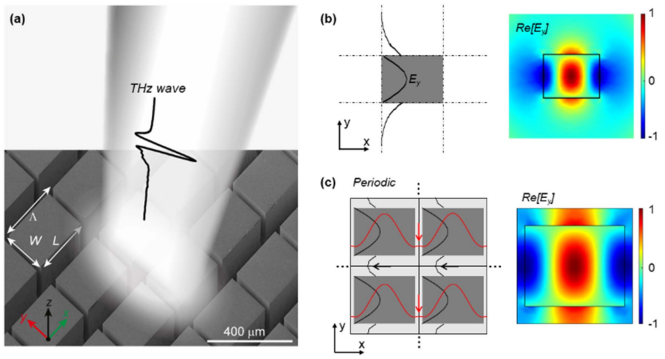

Fig. 1. (a) Perspective SEM images of fabricated all-dielectric metasurface. The THz wave with polarization along y-direction shines from the cubical dielectric resonator side. The geometrical parameters consist of lattice constant Λ, length L along the *x*-axis, and width W along the *y*-axis. (b) An isolated high-contrast cuboid resonator surrounded by air. The right panel shows the real part of the electric field, *y*-component for the TE_2 mode. The left panel shows the electric field (E_y) curve vertically cutting at the middle of the resonator. (c) Periodic resonators array corresponds to the employed high-contrast THz dielectric metasurface. The right panel also shows the real part of the electric field, *y*-component for the TE_2 mode. The red curves in the left panel show the electric field (E_y) curve horizontally cutting at the middle of the resonators, and the black curves show the E_y curves vertically cutting at the middle of the resonators.

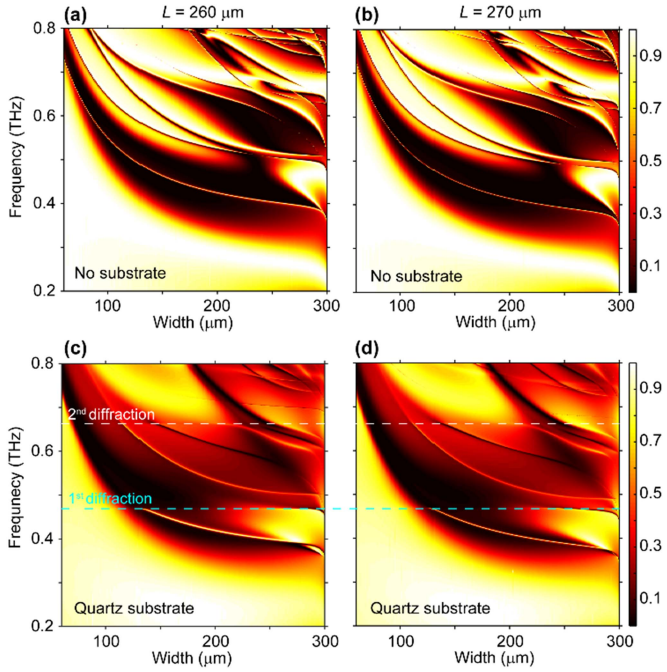

Fig. 2. Transmission maps by varying the geometric width *W* of the resonators in array for the samples with air cladding (suspended array) and quartz substrate. The dominant features for the case with quartz as substrate are the opening of the first (0.47 THz) and second order (0.66 THz) diffraction (Rayleigh anomaly) and the introduced scattering loss due the interface between the resonators and the substrate. (a) and (c) length $L = 260\ \mu$m for samples with air cladding and quartz substrate, respectively. (b) and (d) length $L = 270\ \mu$m for samples with air cladding and quartz substrate, respectively.

perspective for designing low-energy metamaterial and photonic devices towards filling the THz gap [24].

In this work, we have experimentally shown that silicon-based all-dielectric metasurfaces reveal high Q-factors in the THz regime. We investigate the extended Marcatili's analysis in periodic boundary condition in the present system to find that the scaled dimensions along the incident electric field (longitudinal) direction cause redshift of the resonant frequency due to an evanescent wave coupling in the proposed system. However, the resonant Q-factors and amplitudes are mostly the same. Moreover, such extended Marcatili's analysis also illustrates the perturbated electric field with continuous cosine-like filed line along the lateral direction mainly govern the radiation of the presented cuboid-based all-dielectric metasurface. Therefore, the resonant Q-factors can also be manipulated by simple varying the lateral cuboid dimension. The experimental Q-factors of up to 250 was measured. By analysis the resonant Q-factors and resonant frequency distributions, we further discuss that such dielectric metasurface is a suitable platform for THz and/or mid-IR on-chip spectrometers.

II. Results and Discussion

A. Extended Marcatili's Analysis

The cuboids are arranged on a quartz substrate at the nodes of a square lattice with the lattice constant Λ. The samples were fabricated using high-resistivity silicon (>10000 Ω·cm, and $n_{Si} = 3.84$) due to its low-loss and low dispersion at THz frequencies [24]. The scanning electron microscope (SEM) images of fabricated sample are shown in Fig. 1(a). Each individual resonator has a length of *L* in the *x*-direction, width of *W* in the *y*-direction. Numerical simulations are carried out by using commercial finite-element frequency-domain solver COMSOL Multiphysics for the case of normal incident plane wave and TE polarized excitation. The periodic boundary conditions are applied along the *x*-/*y*-directions. A perfect match layer is applied at the input and output ports. Fig. 1(b) shows an isolated cuboid silicon resonator surrounded by air. The extended Marcatili's analysis is applied for such high-index contrast (HIC) configurations [25], [26], as shown in the left panel of Fig. 1(b). For such configuration, the electric field $E_y(x, y)$ with maximum field inside the center of the HIC cuboid resonator is proportional to $e^{ik_z z} cos[k_x(x+\zeta)] cos[k_y(y+\eta)]$ with $k_{x,y,z}$ are the spatial frequencies and ζ, η are the spatial shifts. Outside the core of the HIC cuboid resonator, the field decay exponentially, while the transversal profile of the field is identical to that in the core. Eventually, the field outside the core decays to be zero. Such theoretical framework is confirmed by the calculated eigenmode (electric field, *y*-component), as shown in the right panel of Fig. 1(b). For such isolated resonator, the Q-factor is at the level of 10 that has been experimentally investigated in many micro-nanoparticles made of conventional high-refractive-index semiconductors [17], [18], [20]. For the HIC dielectric metasurface, the fields are expanded onto the Bloch-wave basis: $e^{ik_z z}(\sum_{\boldsymbol{G}} \tilde{\boldsymbol{E}}_{\boldsymbol{G}} e^{i\boldsymbol{G}\cdot\boldsymbol{r}}) cos[k_x(x+\zeta)] cos[k_y(y+\eta)]$, where the middle term in the bracket indicates the Fourier domain, with $\boldsymbol{G} = \hat{x}\, G_x + \hat{y} G_y$ being the Bloch wave number based on the periodicity Λ, and $G_x = 2\,m\pi/\Lambda$, $G_x = 2\,m\pi/\Lambda$, with $m,\ n = 0, \pm1, \pm2, \cdots$, respectively. The extended Marcatili's analysis in periodic boundary condition is shown in Fig. 1(c), where the

$E_y(x)$ in red curve shows a continuous cosine-like oscillations. Between two nearest neighboring HIC cuboids the field curve shows derivation (indicated by the red arrows) that implies the leakage of such configuration. If the horizontal gaps (along x-axis) between the neighboring HIC cuboids close, the field curve becomes continuous cosine oscillations, and the system gives rise to the bound states in the continuum (BICs) [24]. The $E_y(y)$ in back curve shows similar mode profiles as these in the isolated resonator. However, outside the core of the HIC, the field won' t decay to be zero due to the mutual evanescent coupling along the *y*-axis. It should be noticed that such evanescent wave merely radiate energy to the free space. Therefore, manipulating the width (W) of HIC dielectric metasurface can change the resonant frequencies (k_y varies in the HIC cuboid) but the resonant Q-factors are almost the same, which will be numerically investigated and experimentally confirmed in the following contents.

B. Sample Fabrication and Characterization Setup

To fabricate the devices, we followed a five-step fabrication procedure [24], [28]: (1) A 2-μm thick SiO_2 was deposited on the silicon wafer with thickness of 200 μm by the plasma-enhanced chemical vapor deposition (PECVD), where the selectivity of the etching gas ions on silicon and SiO_2 determines the deposition thickness of the SiO_2 layer. (2) The hybrid silicon dioxide-on-silicon wafer was patterned by conventional mask photolithography on SiO_2 with a 500-nm layer of S1805 photoresist. (3) The hybrid silicon dioxide-on-silicon wafer with patterned photoresist was then directly bonded to a 1-mm quartz substrate ($n_{sub} = 2.14$) with a thin layer of spin-coated UV curable polymer optical adhesive (NOA 85) and exposure to UV light (2.5 W/cm^2) for 10 mins. (4) After bonding, the SiO_2 layer was removed by mixed gases of CHF_3 and CF_4 and the remaining pattern is kept as a protective mask for subsequent etching. (5) The silicon wafer was etched by the DRIE (deep reactive ion etching technique; Oxford Estrelas). Each cycle of the Bosch process consists of sidewall passivation (C_4F_8) and etching (SF_6) steps. Each cycle also consists of deposition for 5 s and etching for 15 s. In the deposition step, the C_4F_8 gas (85 sccm) was utilized with 600 W ICP power at 35 mTorr pressure. During the etching step, a mixture of SF_6 (130 sccm) and O_2 (13 sccm) is applied with 600 W ICP power and 30 W bias power, at 35 mTorr pressure. This process cycle was then repeated until the silicon is completely removed. Solid silicon micro-cube arrays were kept attached to the quartz substrate. The periodicities in x- and y-directions are both 300 μm.

The measurements were performed using commercially available terahertz system (TeraScan 1550, Toptica) with frequency-domain spectroscopy. It is a continuous wave-based THz spectroscopy system with high-frequency resolution (10 MHz), which has combined coherent generation and detection of THz radiation in frequency-domain using fiber coupled photoconductive antennas (InGaAs PCAs). Two distributed feedback (DFB) lasers at adjacent frequencies illuminate the photo mixer antennas to generate THz radiation and detect THz signal by measuring the photocurrent at the detector PCA [28]. To resolve the spectral feature of the sample, the frequency was swept from 0.3 THz to 0.6 THz in 10 MHz step size with 100 ms integration time. The measurements were done at room temperature and in the dry nitrogen atmosphere to nullify the effect due to water vapor absorption process.

C. Numerical Results

Fig. 2(a) and (b) show the numerically simulated transmission maps by varying the geometric width (*W*) of the resonators, where the length (*L*) is fixed at 260 μm and 270 μm, and the silicon resonators are cladded with air. By considering quartz as substrate, the A nonzero (*i*, *j*) diffraction channel, known as Rayleigh anomaly, that refers to the appearance or disappearance of diffracted orders into evanescent modes [28], [29], [30], opens at the frequency evaluated by $f = \frac{c}{\Lambda n_{sub}}\sqrt{i^2+j^2}$, where *c* is vacuum light speed, Λ is the lattice constant, n_{sub} is refractive index of quartz substrate. Additional radiation channels result in the overall suppression of zero-order transmission. In our devices, the dominant features are observed at 0.47 THz (first order diffraction labelled as dashed cyan line, $i = \pm 1, j = 0$) and 0.66 THz (second order diffraction labelled as dashed white line, $i = \pm 1, j = \pm 1$), as shown in Fig. 2(c) and (d). Overall, all resonances shift to low frequencies with respect to the increased geometric width for both the air cladding and quartz substrate. Of particular interest is the low-frequency isolated resonance with sharp transparency below the first order diffraction (at 0.47 THz). With the resonator width (*W*) continuously manipulated, the resonance red-shifts proportionally, while the resonant amplitudes (near unit) and Q-factors are merely changed, as shown in Fig. 2. This is due to the non-radiative characteristics of the nearest-neighboring evanescent wave coupling along the oscillation direction of incident THz electric field, as illustrated by the extended Marcatili's analysis in periodic boundary condition for HIC dielectric metasurfaces.

D. Experimental Results

To probe the high-Q resonance in the silicon metasurfaces, we fabricated and analyzed two groups of samples. The geometric parameters of these cavities are length of the cavity $L = 260$ μm, width of the cavity $W = 180$ μm and 210 μm; length of the cavity $L = 270$ μm, width of the cavity $W = 180$ μm and $W = 210$ μm. Fig. 3(a) and (b) exhibit the corresponding numerical and experimental transmitted intensities of the samples with length of 260 μm. Numerically, the extracted Q-factors of the samples are almost same. We extracted the resonance Q-factors from the transmission spectra by using the Fano formula, given by $T_{Fano} = |a_1 + ia_2 + \frac{b}{\omega-\omega_0+i\gamma}|^2$, where a_1, a_2 and b are constant real numbers; ω_0 is the central resonant frequency; γ is the overall damping rate of the resonance [4]. The experimental *Q*-factor was then determined by $Q = \omega_0/2\gamma$, which show similar results. Experimentally, the corresponding Q-factors under Fano fitting are obtained as 163.75 and 102.69, respectively. The experimentally measured resonance frequencies show overall blueshift due to the UV curable adhesive was used to stick the silicon resonators and the quartz substrate. It is clearly observed that both the electric and magnetic fields are highly

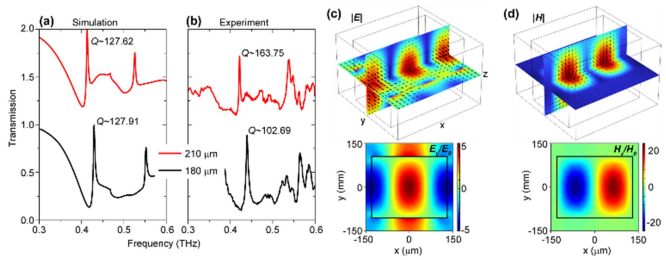

Fig. 3. Numerical simulations and experimental measurements for the samples with fixed geometric length $L = 260$ μm. (a) Numerically simulated and (b) experimentally measured transmission spectra. (c) Top panel: the 3D illustrations of the normalized electric |E| and (d) magnetic |H| fields for the sample with geometric width $W = 210$ μm, where the direction of the back cones indicates the displaced fields correspondingly. Bottom panel: the enhancements of the electric ($Re[E_y]/E_0$) and magnetic ($Re[H_z]/H_0$) field for the sample with geometric width $W = 210$ μm.

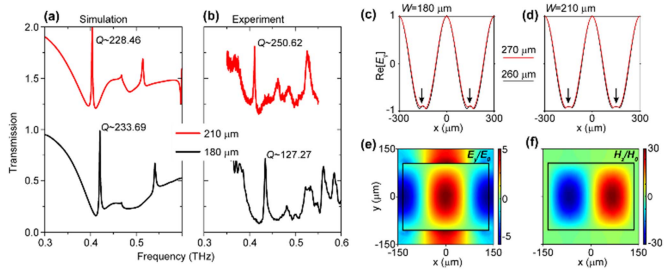

Fig. 4. Numerical simulations and experimental measurements for the samples with fixed geometric length $L = 270$ μm. (a) Numerically simulated and (b) experimentally measured transmission spectra. Electric (E_y) field oscillations along the x-axis for the sample with geo-metric width (c) $W = 180$ μm and (d) $W = 210$ μm, respectively. The black and red curves indicate the comparison of field oscillations between sample $L = 260$ μm (back) and $L = 270$ μm (red), respectively. (e) Electric (E_y) and (f) magnetic (H_z) field enhancements for the sample with geometric length $L = 270$ μm and width $W = 210$ μm. The electric and magnetic fields are normalized to the fields at input port (E_0 and H_0).

enhanced along the lateral direction of the silicon resonators array, as shown in Fig. 3(c) and (d). As explained by the extended Marcatili's analysis in periodic boundary condition, the continuous cosine-like oscillations for both electric and magnetic fields along the lateral (x-axis) direction give rise to the high-Q resonance in the HIC dielectric metasurfaces [19]. The enhanced electric ($Re[E_y]$) and magnetic ($Re[H_z]$) field distributions on xy-plane at the center ($z = 100$ μm) of the resonator, as shown by the bottom panel of Fig. 3(c) and (d), where the sample geometric width is $W = 210$ μm. The magnetic field generated due to the oscillated displacement currents in circulated loops inside the HIC dielectric cuboids, as shown by the top panel of Fig. 3(c) and (d). No in-plane leakage generated by the magnetic fields. Therefore, the relative enhancement of magnetic field ($Re[H_z]$) is much higher than the electric field ($Re[E_y]$), where the electric field provides leakage and lateral coupling for the high-Q resonances to be probed in a way of spectrometric system.

Similarly, the samples with larger geometric length $L = 270$ μm has Q-factor of ~230 that is overall higher than the case with geometric length $L = 260$ μm of the cavity, as shown in Fig. 4. The experimental measurements agree well with the simulations, which also shows overall larger Q-factors than these in Fig. 3. The lateral (x-axis) gap between tow HIC nearest-neighboring cuboid resonators is smaller. As explained by the extended Marcatili's analysis in periodic boundary condition, the continuous cosine-like oscillation for the electric field along the lateral direction is less perturbated, as shown in Fig. 4(c) and (d). It is clearly observed that the electric fields ($Re[E_y]$) along x-axis for devices with geometric parameter of $L = 270$ μm (red curves) are more like a cosine oscillations, as indicated by the black arrows in Fig. 4(c) and (d). However, such field oscillations for the $L = 260$ μm (black curves) get more disturbed. Once again, the distortion in the cosine-like field oscillation provides the radiation channels for the HIC dielectric metasurfaces, thereby making the resonance to be leaky. The relative enhancements of the electric field ($Re[E_y]$) and magnetic field ($Re[H_z]$) for the sample $L = 270$ μm, $W = 210$ μm are shown in Fig. 4(c) and (d), which further prove the extended Marcatili's analysis proposed in this work.

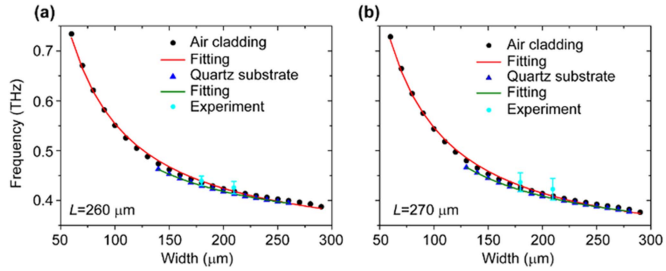

Fig. 5. Fitting of the low-frequency resonance mode with exponential equation. (a) Length $L = 260$ μm for samples with air cladding and quartz substrate, respectively. (b) Length $L = 270$ μm for samples with air cladding and quartz substrate, respectively.

E. Evanescent Wave Coupling-Induced Frequency Shift

We use an exponential equation as a function of cavity width W to fit the trajectory of the transmission peaks of the interested resonances, as shown in Fig. 5. It is clearly observed that the resonance trajectory is well fitted by the exponential equation as the evanescent wave coupling has character of exponential decay. Above the first order diffraction channel, the resonance in the experimental spectra is invisible for the samples with quartz substrate. Below the first order diffraction channel, the resonance frequency has slight divergence compared to the samples with air claddings, and then it converges as the width of the resonator approaches 300 μm in which case all the cubes in the x-direction touch each other forming continuous grating. The main reason is that the interface between the silicon resonators array and the quartz substrate can distort the electric and magnetic fields at their interfaces. However, this interface effect becomes small as the filling factor increases, i.e., the geometric width increases and becomes a grating pattern [24]. It should be noticed that the key geometric parameters lattice constant (Λ), length (L) and width (W) of the dielectric cuboid resonators can be globally scaled. Therefore, the high-Q resonances with different frequencies can be fabricated to give rise to a barcoding distribution that can cover a wideband region [32], [33], [34], [35], [36], [37]. As

discussed above, the design shown in this work only has electric field penetrates to the surrounding air. As a result, the fingerprints of organic gases, liquids, and solids can be sensed by such electric field penetrations. An on-chip spectrometric bio-sensor could be generated by the current design [32], [33].

III. Conclusion

In summary, we have experimentally demonstrated terahertz all-dielectric high-Q metasurfaces that show strong field confinement. We applied the extended Marcatili's analysis in periodic boundary condition for the proposed metasurface to find that the longitudinal evanescent wave coupling along the oscillating direction of electric field doesn't radiate EM energy. Therefore, the resonant frequencies have been exponentially shifted by simply modulating the longitudinal geometric dimension, while the resonant Q-factors and amplitude are merely changed. Our results provide an efficient method for designing high-Q all-dielectric meta-devices, that could functionalize as on-chip spectrometer for molecular fingerprint sensors in the terahertz and mid-IR regime. The simple design can also be scaled down to nanoscale for optical applications, such as low threshold nano-lasers, on-chip parametric amplifiers, and harmonic generators.

References

[1] A. Kodigala, T. Lepetit, Q. Gu, B. Bahari, Y. Fainman, and B. Kanté, "Lasing action from photonic bound states in continuum," *Nature*, vol. 541, pp. 196–199, 2017.

[2] J. S. Totero Gongora, A. E. Miroshnichenko, Y. S. Kivshar, and A. Fratalocchi, "Anapole nanolasers for modelocking and ultrafast pulse generation," *Nature Commun.*, vol. 8, 2017, Art. no. 15535.

[3] H. Zhang et al., "Biosensing performance of a plasmonic-grating-based nanolaser," *Prog. Electromagn. Res.*, vol. 171, pp. 159–169, 2021.

[4] Y. Yang, I. I. Kravchenko, D. P. Briggs, and J. Valentine, "All-dielectric metasurface analogue of electromagnetically induced transparency," *Nature Commun.*, vol. 5, 2014, Art. no. 5753.

[5] Y. Yang et al., "Nonlinear Fano-resonant dielectric metasurfaces," *Nano Lett.*, vol. 15, 2015, Art. no. 7388.

[6] S. Liu et al., "Resonantly enhanced second-harmonic generation using III–V semiconductor all-dielectric metasurfaces," *Nano Lett.*, vol. 16, pp. 5426–5432, 2016.

[7] G. Grinblat, Y. Li, M. P. Nielsen, R. F. Oulton, and S. A. Maier, "Enhanced third harmonic generation in single germanium nanodisks excited at the anapole mode," *Nano Lett.*, vol. 16, pp. 4635–4640, 2016.

[8] A. S. Shorokhov et al., "Multifold enhancement of third-harmonic generation in dielectric nanoparticles driven by magnetic Fano resonances," *Nano Lett.*, vol. 16, pp. 4857–4861, 2016.

[9] T. Shibanuma, G. Grinblat, P. Albella, and S. A. Maier, "Efficient third harmonic generation from metal-dielectric hybrid nanoantennas," *Nano Lett.*, vol. 17, pp. 2647–2651, 2017.

[10] Z. Liu et al., "High-Q quasibound states in the continuum for nonlinear metasurfaces," *Phys. Rev. Lett.*, vol. 123, 2019, Art. no. 253901.

[11] B. B. Li, W. R. Clements, X. C. Yu, K. Shi, Q. Gong, and Y. F. Xiao, "Single nanoparticle detection using split-mode microcavity Raman lasers," *Proc. Nat. Acad. Sci. USA*, vol. 111, 2014, Art. no. 14657.

[12] M. L. Brongersma, Y. Cui, and S. Fan, "Light management for photovoltaics using high-index nanostructures," *Nature Mater.*, vol. 13, pp. 451–460, 2014.

[13] O. Hess, J. B. Pendry, S. A. Maier, R. F. Oulton, J. M. Hamm, and K. L. Tsakmakidis, "Active nanoplasmonic metamaterials," *Nature Mater.*, vol. 11, pp. 473–484, 2012.

[14] N. Wu, Y. Zhang, H. Ma, H. Chen, and H. Qian, "Tunable high-Q plasmonic metasurface with multiple surface lattice resonances," *Prog. Electromagn. Res.*, vol. 172, pp. 23–32, 2021.

[15] L. Liu and Z. Li, "Spoof surface plasmons arising from corrugated metal surface to structural dispersion waveguide," *Prog. Electromagn. Res.*, vol. 173, pp. 93–127, 2022.

[16] F. Ding, "A review of multifunctional optical gap-surface plasmon metasurfaces," *Prog. Electromagn. Res.*, vol. 174, pp. 55–73, 2022.

[17] S. Jahani and Z. Jacob, "All-dielectric metamaterials," *Nature Nanotechnol.*, vol. 11, pp. 23–36, 2016.

[18] A. I. Kuznetsov, A. E. Miroshnichenko, M. L. Brongersma, Y. S. Kivshar, and B. Lukyanchuk, "Optically resonant dielectric nanostructures," *Science*, vol. 354, 2016, Art. no. aag2472.

[19] I. Staude and J. Schilling, "Metamaterial-inspired silicon nanophotonics," *Nature Photon.*, vol. 11, pp. 274–284, 2017.

[20] A. E. Miroshnichenko et al., "Non-radiating anapole modes in dielectric nanoparticles," *Nature Commun.*, vol. 6, 2015, Art. no. 8069.

[21] C. Wu et al., "Spectrally selective chiral silicon metasurfaces based on infrared Fano resonances," *Nature Commun.*, vol. 5, 2014, Art. no. 3892.

[22] Y. Shen, V. Rinnerbauer, I. Wang, V. Stelmakh, J. D. Joannopoulos, and M. Soljacic, "Structural colors from Fano resonances," *ACS Photon.*, vol. 2, pp. 27–32, 2015.

[23] M. Tonouchi, "Cutting-edge terahertz technology," *Nature Photon.*, vol. 1, pp. 97–105, 2007.

[24] S. Han et al., "All-dielectric active terahertz photonics driven by bound states in the continuum," *Adv. Mater.*, vol. 31, 2019, Art. no. 1901921.

[25] E. Marcatili, "Dielectric rectangular waveguide and directional coupler for integrated optics," *Bell Syst. Tech. J.*, vol. 48, pp. 2071–2121, 1969.

[26] W. J. Westerveld, S. M. Leinders, K. W. A. van Dongen, H. P. Urbach, and M. Yousefi, "Extension of Marcatili's analytical approach for rectangular silicon optical waveguides," *J. Light. Technol.*, vol. 30, no. 14, pp. 2388–2401, Jul. 2012.

[27] S. Han, M. V. Rybin, P. Pitchappa, Y. K. Srivastava, Y. S. Kivshar, and R. Singh, "Guided-mode resonances in all-dielectric terahertz metasurfaces," *Adv. Opt. Mater.*, vol. 8, 2019, Art. no. 1900959.

[28] A. J. Deninger, A. Roggenbuck, S. Schindler, and S. Preu, "2.75 THz tuning with a triple-DFB laser system at 1550 nm and InGaAs photomixers," *J. Infrared, Millimeter, THz Waves*, vol. 36, pp. 269–277, 2015.

[29] U. Fano, "The theory of anomalous diffraction gratings and of quasi-stationary waves on metallic surfaces (Sommerfeld's waves)," *J. Opt. Soc. Amer.*, vol. 31, pp. 213–222, 1941.

[30] S. S. Wang and R. Magnusson, "Theory and applications of guided-mode resonance filters," *Appl. Opt.*, vol. 32, pp. 2606–2613, 1993.

[31] G. Quaranta, G. Basset, O. J. Martin, and B. Gallinet, "Recent advances in resonant waveguide gratings," *Laser Photon. Rev.*, vol. 12, 2018, Art. no. 1800017.

[32] A. Tittl et al., "Imaging-based molecular barcoding with pixelated dielectric metasurfaces," *Science*, vol. 360, pp. 1105–1109, 2018.

[33] F. Yesilkoy et al., "Ultrasensitive hyperspectral imaging and biodetection enabled by dielectric metasurfaces," *Nature Photon.*, vol. 13, pp. 390–396, 2019.

[34] H. Hu et al., "Catalytic metasurfaces empowered by bound states in the continuum," *ACS Nano*, vol. 16, pp. 13057–13068, 2022.

[35] J. Wang, T. Weber, A. Aigner, S. A. Maier, and A. Tittl, "Mirror-coupled plasmonic bound states in the continuum for tunable perfect absorption," 2022, *arXiv:2211.03673*.

[36] T. Shi et al., "Planar chiral metasurfaces with maximal and tunable chiroptical response driven by bound states in the continuum," *Nature Commun*, vol. 13, 2022, Art. no. 4111.

[37] Z. Hu, N. He, Y. Sun, Y. Jin, and S. He, "Wideband high-reflection chiral dielectric metasurface," *Prog. Electromagn. Res.*, vol. 172, pp. 51–60, 2021.